Metallic Behavior in STO/LAO Heterostructures with Non-Uniformly Atomic Interfaces

Rafael A.C. Amoresi[1,2*], Leonélio Cichetto Jr.[2,3], Amanda F. Gouveia[4], Yormary N. Colmenares[5], Marcio D. Teodoro[3], Gilmar E. Marques[3], Alexandre Z. Simões[1], Juan Andres[2], Elson Longo[4], Adenilson J. Chiquito[3], Maria A. Zaghete[6]

[1]*Faculty of Engineering of Guaratinguetá, São Paulo State University – UNESP, 12516-410, Guaratinguetá, SP, Brazil*

[2]*Department of Analytical and Physical Chemistry, University Jaume I (UJI), Castello 12071, Spain*

[3]*Department of Physics Federal University of São Carlos - UFSCAR, 13565-905 São Carlos, SP, Brazil*

[4]*CDMF, Federal University of São Carlos - UFSCAR, 13565-905 São Carlos, SP, Brazil*

[5]*Institute of Physics of São Carlos, University of São Paulo - USP, 13560-970, São Carlos, Brazil*

[6]*Interdisciplinary Laboratory of Electrochemistry and Ceramics, LIEC – Chemistry Institute, São Paulo State University – UNESP,14800-060, Araraquara, SP, Brazil*

ABSTRACT

The search for new and low-power switching devices involving the integration of semiconductor thin films is of interest, and has led to renewed research because such devices may exhibit innovative properties. Here, we investigate the two-dimensional electron gas (2DEG) at the $LaAlO_3/SrTiO_3$ interface with metallic and insulator behavior. Insight is offered by quantifying the interface charge distribution associated with structural and electronic order-disorder effects. Variations in the electron conductivity were observed to be associated with different specific clustering arrangements of both Ti and Al cations of the co-exposed surfaces at the interface, i.e., structural and electronic connectivity among the undercoordinated $[TiO_5]$ and $[AlO_5]$ clusters. These results indicate facet control as a strategy for enhancing the electric and magnetic properties of a device via the quantum confinement of electrons.

Keywords: $LaAlO_3/SrTiO_3$ interface, Two-dimensional electron gas (2DEG), Thin film oxygen pressure, Electronic transport properties, DFT calculations

1. INTRODUCTION

The large number of studies on materials with heterojunctions generated by the co-exposed surfaces of the ABO_3 perovskite structure reflects the considerable research interest in these compounds. Their unique physico-chemical behavior and stability make them particularly appealing for a variety of technological applications. In particular, confined materials involving an atomically thin two-dimensional electron gas (2DEG) of perovskite heterostructures with structural anisotropy, rich surface chemistry, and unique electronic structures, are technologically intriguing because they exhibit fascinating changes and unusual behavior vis-à-vis their corresponding free state counterparts.[1–12]

Since the first report by Hwang and Ohtomo[13] on the 2DEG at the interface of two otherwise insulating metal oxides, $SrTiO_3$ (STO) and $LaAlO_3$ (LAO), the LAO/STO heterostructure has been studied extensively owing to novel phenomena that are associated with the confinement of correlated electrons at the interface. (H. Lee, N. Campbell, J. Lee, T. J. Asel, T. R. Paudel, H. Zhou, J. W. Lee, B. Noesges, J. Seo, B. Park, L. J. Brillson, S. H. Oh, E. Y. Tsymbal, M. S. Rzchowski and C. B. Eom, Nat. Mater., 2018, 17, 231–236. A. K. Singh, T.-C. Wu, M.-C. Chen, M.-Y. Song, W.-L. Lee, C.-P. Su and M.-W. Chu, Phys. Rev. Mater., 2018, 2, 114009).

Stimulating Oxide Heterostructures: A Review on Controlling SrTiO3-Based Heterointerfaces with External Stimuli

Por: Christensen, DV (Christensen, Dennis Valbjorn)[1]; Trier, F (Trier, Felix)[2]; Niu, W (Niu, Wei)[1,3,4]; Can, YL (Can, Yulin)[1]; Zhang, Y (Zhang, Yu)[1,5,6]; Jespersen, TS (Jespersen, Thomas Sand)[7]; Chen, YZ (Chen, Yunzhong)[1]; Pryds, N (Pryds, Nini)[1]

Ver número de ResearcherID y ORCID de Web of Science

ADVANCED MATERIALS INTERFACES

Volumen: 6

Número: 21

Número de artículo: 1900772

Several studies have revealed the wide range of technological applications of the heterostructure, such as in electronic devices,[14] superconductors,[15] and spintronics.[16] Understanding the properties and stability of these materials is the key to maximizing the impact of materials engineering.[17–19] Therefore, the ability to control both the atomic structure and composition of these oxide layers formed by ABO_3-based materials, as well as their interfaces, is emerging as one of the major challenges in the development of electronic devices with a range of functional properties.

With the advent of state-of-the-art thin-film deposition techniques, such as pulsed laser deposition (PLD), atomically sharp interfaces can be manufactured.[20–23] Since oxidizing or reducing conditions can change the properties of the 2DEG, it is important to verify the actual impact under real operating conditions; then, the effect of the presence of oxygen can be investigated. It is also important to understand this phenomenon at a more fundamental level. Therefore, we set up the basis for further analysis of the experimental results with a theoretical picture of the electron system for the 2DEG at the LAO/STO interface. Ultimately, it is necessary to clarify these open questions not only because of their academic value, but also because of their key roles in understanding other systems that might show similar behaviors and how they could be utilized. Consequently, we revisited the origin of the 2DEG and further explored new ways of tuning its properties, based on a detailed density functional theory (DFT) study. Our results are expected to provide new knowledge about this type of interface system.

The main objective of the present work is to show that the electrical conductivity phenomena of interface are related to the interaction of arrangement of atomic clusters. Considering the constraints imposed by the two-dimensional conduction nature for the existence of the gas and the electron-electron correlation, we will investigate the properties of the 2DEG on the LAO/STO interface based on two carefully designed systems, metallic and insulator systems. LAO/STO films were obtained using PLD, and the underlying physical and chemical reasons for the 2DEG observation are discussed based on results from X-ray

photoelectron spectroscopy, photoluminescence (PL) emissions, and temperature-dependent (magneto) transport measurements. To complement and rationalize the experimental results, first-principles DFT calculations were employed to obtain information at the interface between the LAO/STO heterojunction. To this end, structural analysis of the electron transfer process and monitored Mullikan charges calculations were performed to understand the structural and electronic order-disorder effects on the formation of 2DEG, providing new insight into the properties of this material. We complement these calculations with an investigation of the local coordination of La, Al, Sr, and Ti cations, i.e., the under-coordinated clusters on the surfaces, to propose an atomic-level model to provide insight and understand the origin of the 2DEG phenomena. We provide evidence that this is due to the interaction of the local coordination of these cations on the co-exposed surfaces at the heterojunction. The results presented in this work are expected to improve the performance of the 2DEG $LaAlO_3/SrTiO_3$ interface.

The paper is organized as follows. In the next section, an overview is provided, in which the more relevant experimental and theoretical results in the literature are emphasized. Our results are discussed in four separate subsections within Section 3: transport properties, structural and electronic order-disorder effects at the interface, and joint theoretical and experimental analysis of the formation process of the 2DEG. The main conclusions are summarized in Section 4. In Section 5 the experimental methods are presented, comprising three subsections: the growth process of the LAO/STO interface, characterization techniques, and electrical and magnetic measurements.

2. OVERVIEW

The observation of a high charge mobility due to the presence of a 2DEG at the LAO/STO heterostructure has attracted widespread interest and motivated many studies that have attempted to find the origin and nature of the conductivity at the interface.[24–26] In addition, many other physical properties, not found in their bulk counterparts, have also been observed.[14,15,27–

[33] At the interface between of the LAO/STO heterostructure, a 2DEG of high mobility ($10^3 cm^2V^{-1}s^{-1}$)[5,19] has been observed. Electrons move freely along an in-plane direction of the heterostructure interface while they are confined within a few nanometers of out-of-plane direction from the interface.[13] Studies have shown that there are electric and magnetic moment interactions with the neighboring atomic layers between STO and LAO.[6–8] In addition, a 2DEG has been observed on interfaces involving STO with ABO_3/STO (*A* = La, Pr, Nd and *B* =Al, Ga)[34–37] and $LaFeO_3$[38] as an ultrathin epitaxial film. The processes generated by the presence of the 2DEG at the LAO/STO heterostructure can be considered assignature of a particular behavior of these interfaces, involving electronic band alignment that controls electron transport, the mechanical strain that changes the local electronic structure, and chemical bonding with the concomitant formation of new electronic states as active centers for trapping electrons and/or ions.[39–42] However, there is a lack of consensus regarding the nature and formation of the 2DEG, as different scenarios have been employed to rationalize this phenomena based on three main aspects: oxygen vacancies; structural deformation involving cation disorder; and electronic and orbital interface reconstruction.[43–47]

DFT calculations using explicit atomistic models of the interface, have been extensively made for understanding the geometry and electronic properties of the LAO/STO interface. In this case, a polarity mismatch occurs at a polar–nonpolar interface of two oxide insulators, LAO and STO, and such an electrostatic discontinuity can drive an electronic/atomic reconstruction.[48] In real material systems, non-stoichiometry can coexist with polarity mismatch, but how they interact with each other and affect the electronic and magnetic properties is still unclear.[24,49,50] Therefore, an understanding of the interaction between non-stoichiometry and polar mismatch at the atomic level is necessary.[51,52] Usually, the nature of a semiconductor heterojunction is analyzed by looking at the band edges of the separate and interacting fragments, and the localization of holes and electrons in the interface associated with the process of charge carrier separation.[53] A plethora of simulations of LAO thin film on an

STO substrate with *vacuum* on top of LAO have been performed to explain the conductivity associated with the formation of 2DEG at the LAO/STO and related interfaces.[47,54–71]

The simulations are based on the construction of computational models with different interface combinations $(LaO)^{+}$–$(SrO)^{0}$, $(LaO)^{+}$–$(TiO_2)^{0}$, $(AlO_2)^{-}$–$(TiO_2)^{0}$, or $(AlO_2)^{-}$–$(SrO)^{0}$ surface termination. Recently, Guan et al.[72], studied the different models of LAO/STO heterostructures with a focus on the electronic properties of the interfaces and the influence of the geometry of the models on theoretical results. These simulations, based on the results of theoretical high-throughput methods, are capable of providing a direct comparison between experimental data and theoretical results. Furthermore, they provide a deeper insight, at the atomic level, that can be used to further determine the mechanism of 2DEG conductivity from the perspective of first-principles calculations. The identification of appropriate combinations of materials, explorations of new mechanisms, and then the practical realization of these interfaces should result in new technological applications.

To explain the origin of the 2DEG behavior, different mechanisms have been invoked based on the LaO/TiO_2-terminated (001) interface that are related to the polar $(LaO)^{+}$ and neutral $(TiO_2)^{0}$ planes joined at the interface.[12,13,27] They include the following: (i) a polar catastrophe mechanism in which the charge transfer process takes place from the polar $LaAlO_3$ to the nonpolar $SrTiO_3$ layers at the interface;[25] (ii) an oxygen vacancy-induced mechanism in the STO or LAO layers;[43,73–76] (iii) interdiffusion of interfacial cations to form an La/Sr interfacial mixing;[44,77–80] (iv) a mechanism related to the defect-free electronic reconstruction mechanism, in which Ti mixed valence states appear at the $(LaO)^{+}/(TiO_2)^{0}$ termination;[45] and (v) a mechanism related to charge-compensating defects formed by cationic vacancies.[81] However, it is increasingly evident that other LaO/TiO_2-terminated interfaces, terminated along the (110) and (111) surfaces instead of the (001) surface of LAO/STO interfaces, although having different polar natures, have similar conducting interfaces.[46,82] Recent studies reveal that non-uniform atomic terminations between $(AlO_2)^{-}/(SrO)^{0}$ atomic planes also presente conducting

mechanisms.[Lee-2018, Direct observation of a two-dimensional hole gas at oxide interfaces, Nature Materials, v.17, 231-236, 2018] This be related to the fact that the growth of the atomic layers is not based on a perfect long-range stoichiometry of the ions at the interface.[19,77,78,83,84] Furthermore, calculations show that the AlO_2 layer plays an important participation at the interface,[56,85][Warusawithana-2013, LaAlO3 stoichiometry is key to electron liquid formation at LaAlO3/SrTiO3 interfaces NATURE COMMUNICATIONS | 4:2351 | DOI: 10.1038/ncomms3351] which together with its thermodynamic surface instability compared to LaO,[86,87] marks it as an important part of the STO/LAO interface. These results pave the way to a new line of research, as they indicate that the interfacial atomic arrangement in LAO/STO interfaces is paramount, particularly in cases where the subsequent electronic properties of the material exhibit geometrical preferences along polar and/or crystallographic directions that feature inevitably complex surface reconstructions. Therefore, the nature of the mechanism of the interfacial conduction is still an open question and remains a key puzzle for these interfaces.[88–90] These findings prompt careful studies of the initial surfaces of perovskite film growth to correlate the physical behavior of the film with its interfacial structure.

3. RESULTS AND DISCUSSION

3.1 Transport Properties

Temperature-dependent resistance curves R(T) of samples obtained are shown in Figures 1a,b. Different regions of the samples were analyzed, as shown in inset of figure. Here, an AC current excitation (100 nA – 1 μA) was applied to the outer electrodes, and the longitudinal resistance was measured between two inner potentiometric probes along the current direction. Data exhibit metallic behavior for oxygenated sample, Figure 1a. It is observed from literature that the heterostructured samples growth along different mechanisms; in some works the films are cooled by oxidation processes[15,91] and others use the same deposition pressure.[13,14] In this sense, the second sample set was tested without the oxidation stage while cooling (non-oxygenated sample), Figure 1b.

The curves for electrodes A to D for this sample set exhibit two distinct slope regions, which we assigned to two distinct conduction mechanisms. The point of transition is ~125 K. Above this point, a metallic character is observed [92] and below 125 K, the resistance data show an insulating character. Then, the set of non-oxygenated samples shows metal-to-insulator transition behavior. Published works by Kalabuklov et al.[73,93] have shown that the chemical environment of the heterostructure is very sensitive to obtain metallic or insulator behavior. Magnetoresistance measurements (Figure 1c) were made between electrodes A to D for sample that showed only metallic characteristics, oxygenated samples, and a significant range of magnetoresistance was observed at 4 K, and it decreased as the temperature increased, and it is implies a characteristic for the presence of 2DEG.[94–96]

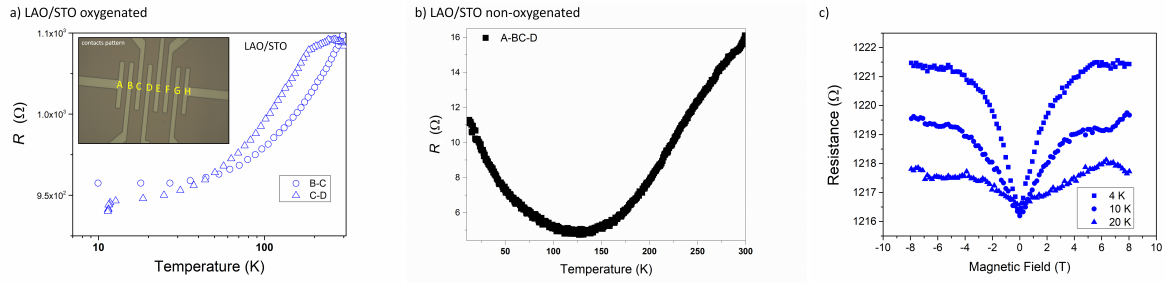

Figure 1. Transport curves for the sample sets without and with the oxygenation step: measurements of the temperature dependent resistance for a) oxygenated and b) non-oxygenated films (inset: the contact patterns used); c) Magnetoresistance curves in which a magnetic field is applied at ± 8 Tesla at 4 K, 10 K, and 20 K at electrodes A through D of the oxygenated film.

3.2 Structural and electronic order-disorder effects at the interface

In order to understanding why the oxygenated and non-oxygenated samples show metallic and insulating behavior, respectively, morphological and structural analysis were performed.

AFM measurements (Figure S1) indicate lack of the typical structure of terrace-step to the epitaxial growth of films. Raman spectroscopy (Figure S2a) and XRD analysis (Figure S2b) were performed to investigate both short and long-range structural order, respectively. Raman spectroscopy, Figure S1b, shows in a different way than previously reported in the literature, the interface interactions between adjacent clusters. Figure S2b shows the long-range analysis by XRD in which both systems, oxygenated and non-oxygenated, have peaks related to the cubic phase of the STO monocrystal, confirming the texturing of the films; however, to non-oxygenated sample the presence the others peaks, suggest the coexistence of secondary phases. In order to analyze the surface composition of the samples, XPS analyses were performed. Comparing the quantitative results for atomic concentrations (Table 1), a significant difference is noted between the stoichiometries of the samples. The atomic concentration ratio Sr/Al or Ti/La is higher for oxygenated samples. It is suggested that the oxygenation of the system during the growth of the films increases the interdiffusion of the atoms of Sr and Ti in the heterostructure and consequently changes the chemical environment in the heterostructure [Lee-2016, Hidden lattice instabilities as origin of the conductive interface between insulating LaAlO3 and SrTiO3 NATURE COMMUNICATIONS | 7:12773 | DOI: 10.1038/ncomms12773]. In addition, the composition of Al appears higher for the oxygenated sample, which shows a metallic behavior, and different from that observed by Sato et al. [Sato-2013_Stoichiometry control of the electronic, Appl. Phys. Lett. **102**, 251602 (2013); https://doi.org/10.1063/1.4812353] which demonstrates that the non-stoichiometry of the films results in a change in electrical conductivity, not observed in our samples. This difference is accompanied by a small shift of the Al 2p peak ($\Delta E = 0.36$ eV) in the oxigenated sample, shown by the high-resolution XPS spectra for both samples are shown in Figures 2 and 3, respectively.

The energy peaks associated with the upper part of the heterostructure, corresponding to the core levels Al2p and La 3d of the LAO unit cells, are shown in Figure 2. The binding energies for lanthanum and aluminum on the samples surface correspond to the reported results for Al^{3+} and La^{3+} oxidation states. These findings in intensity/position were already reported in

the literature.[83,97] Qiao et al.[83] observed that, for the La $4d$/Al $2p$ peak area ratios, equal intensities were obtained when comparing stoichiometric films with LAO single crystals. They reported that the difference in intensity is due to stoichiometric differences. Drera et al. (2012)[97] also observed a difference in the intensity of the La $4d$ peaks. They observed that samples presenting the highest peak intensity will be insulators, suggesting that the oxygen deposition pressure has a relevant effect on the cation stoichiometry during the formation of the film. We observed variations in both the shift of the $2p$ peaks and intensity of the La $3d$ peak (Figure 3b). This may be attributed to a lower oxidation state,[98] or alteration of the chemical environment related to the electron distribution around the ion.

Table 1. Relative atomic composition of oxigenated and non-oxigenated samples.

					Composition		Interdiffusion	
Sample	Ti % (±0.2)	Sr % (±0.2)	La % (±0.2)	Al % (±0.2)	Ti/Sr	Al/La	Sr/Al	Ti/La
Non-oxygenated	0.5	4.8	33.6	61.1	0.1	1.8	0.08	0.01
Oxygenated	1.2	10.4	24.3	64.0	0.1	2.6	0.16	0.05

Studying the effects of oxidation states, Palacio et al.[98] observed a minimum variation of 1.2 eV, whereas we have observed one of 0.3 eV (Al $2p$ peak), which also ruled out the possibility of a change in the oxidation state of Al. However, bond energy variation as a result of the chemical environment is perfectly plausible; the structure of the films has a complex oxide configuration, and there are different studies[99,100] showing that different coordination geometries can be achieved. The octahedral environments have smaller binding energies than the tetrahedral environments without any changes in oxidation state.[99,101,102] We believe that this observation is consistent with our study.

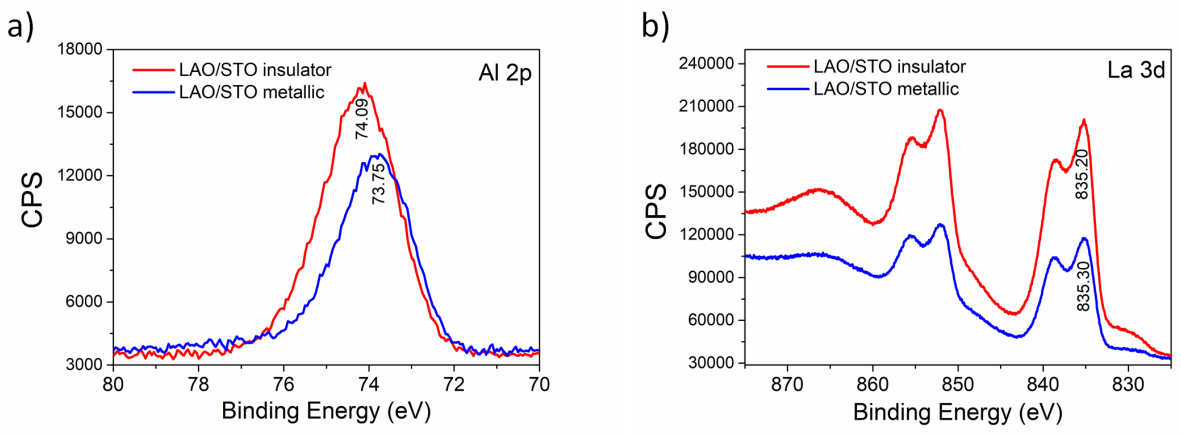

Figure 2. XPS spectrum for a) Al 2p and b) La 3d collected from metallic and insulator systems. The spectra for Al 2p show a shift toward lower binding energy for the metallic system, and for the spectra of La 3d, a higher intensity for the insulator system compared to the metallic system.

Titanium cations at the interface region of samples are detectable by XPS owing to the few LAO unit cells above them. Studies have shown[103,104] the existence of aTi^{3+} state that appears as a shoulder at lower energies on the line $2p_{3/2}$ next to the main peak of Ti^{4+}. The authors suggested that the Ti^{3+} component is only present in the first monolayers near the interface,[104,105] and that this oxidation state is associated with the occupation of $3d$ empty states of Ti.[36] These cations would diffuse into the interface and then cause the high charge mobility.[103,106] However, Chambers et al.[78] have shown that the charges of ions that diffuse at the interface (Ti/Al and Sr/La) are completely compensated for, resulting in an invariance of the Ti oxidation state. The Ti $2p$ core levels of both samples are shown in Figure 3a and 3c.

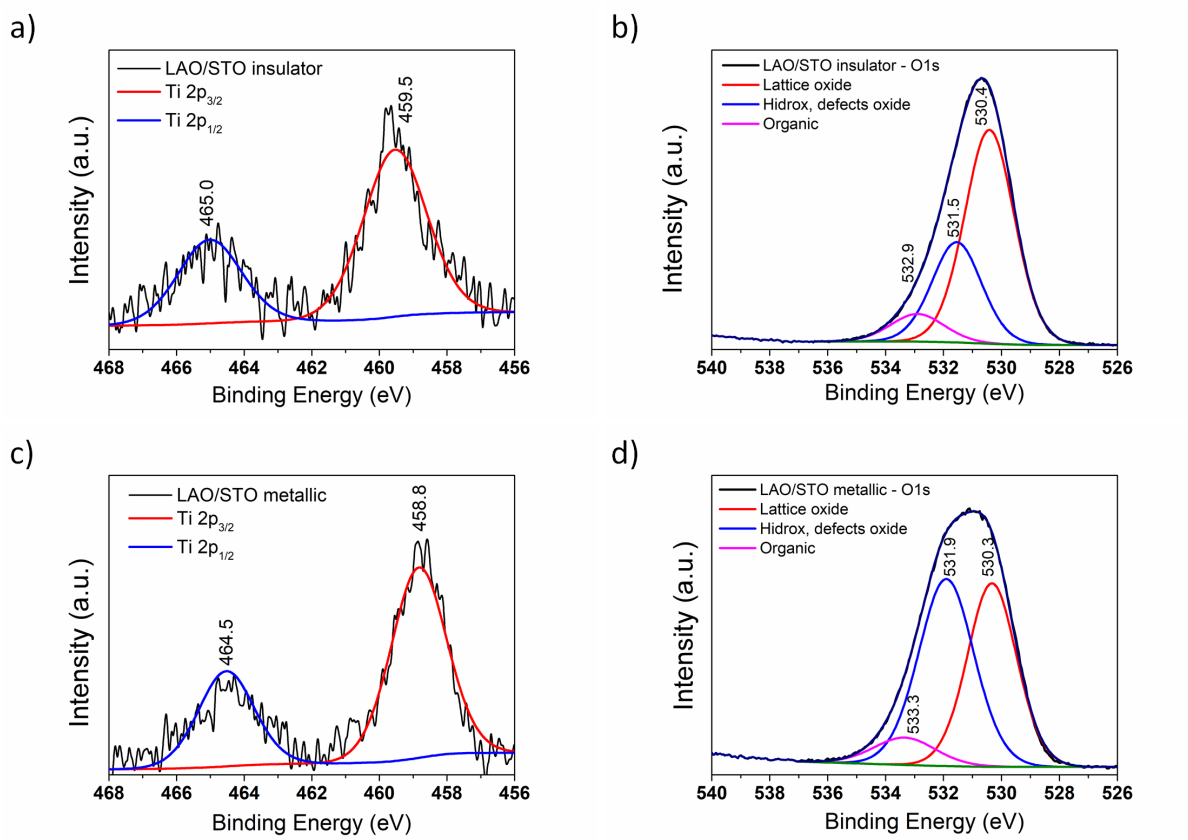

Figure 3. XPS spectrum for (a, c) Ti 2p and (b, d) O 1s for the insulator and metallic system, respectively. The spectra show an oxidation state of +4 for Ti with variation for lower binding energy for the metallic system. The O1s spectra show an increase in the area corresponding to oxygen vacancies for the oxygenated system.

The insulator system, non-oxygenated, has a Ti bonding energy, $2p_{3/2}$, centered at 459.5 eV, while for the oxygenated system, it is shifted to 458.8 eV, a variation in the lower binding energy of -0.7 eV. Both values correspond to the +4 oxidation state of Ti. However, the lower binding energy for Ti in the metallic system indicates an increase in electron density.[107] Considering the full width at half maximum (FWHM) of the fitted peaks Ti$2p_{3/2}$ (~2eV) and the asymmetry of the experimental core level, it is possible to consider the presence of Ti in more than one oxidation state. Nevertheless, the experimental limitations of noise signal ratio, does not allow the proper fitting of Ti $2p$ with two oxidation states.

The O 1s peak for the two systems shows different symmetries, Figure 3b and 3d. The insulator system, non-oxygenated, presents sharp and asymmetric peak shape while the metallic system exhibits a broad and symmetric peak shape. The O 1s level is adjusted with three components each assigned from the highest to lowest binding energy: i) organic groups $–CO_3$, H_2O adsorbed, or O_2 adsorbed (~533 eV); ii) regions of oxygen deficiency compared to the matrix (~531 eV); and iii) the lattice oxygen (~530 eV).[108–112] For the metallic system, the corresponding areas of the oxygen deficiency regions increase (49.14%) in comparison to those of the insulator system (29.14%). This region corresponds to a chemical environment with complex clusters disordered by the interatomic distance, bond angle, and dihedral angle that cause changes in the electronic density such that it is less localized than those of the dipoles. This effect is accentuated by the presence of oxygen vacancies in these clusters.

Therefore, considering the large number of defects in the structural environment, these can be related to the O 1s peak. At the same time, for the energy shift of lower binding energies for the Al 2p and Ti 3d peaks in the metallic system, it can be assumed that during the growth of films, at low oxygen pressures, there is a heavy contribution of tetrahedral clusters and that after oxygenation there is a large stabilization of the octahedral clusters (verified through an analysis of the energy of the cations' chemical environment) for Ti in the coordination of the films. It could be argued that the remaining defects of the structure correspond to both parts of the interface (Sr,Ti, / La/Al); however, for the metallic system (oxygenated sample), the contribution of Ti and Sr is higher compared to the insulator system (non-oxygenated sample). For this reason, the presence of different types of clusters of Ti, as the lattice former, should be considered at the interface region. This analysis leads us to believe that octahedral and tetrahedral clusters are present on the surface of the substrate during the LAO deposition. Enterkin et al. [113], when studying the surface of STO, have also reported the possibility of the presence of these two types of clusters.

Accordingly, 2DEG formation process can be associated and explained by order–disorder degree of the materials, and to this end, PL emissions in which its profile is a typical multiphonon process, were analyzed in the range from 10 to 300 K (Figure 4).[114] The two systems share similar PL characteristics. Both have high intensity emissions in the green region of 495–570 nm at low temperatures. The metallic system has a slightly shifted emission center at 2.32 eV (10 K) compared to the insulator system at 2.38 eV (10 K), ΔE = − 60 meV. PL emissions for the STO substrate show a low intensity signal. This is expected, as the PL emissions of oxides are generated by structural disorder,[114,115] while the STO substrate is a single crystalline material. However, the intensity of the PL emissions of heterostructure samples is very intense owing to the presence of defect levels at the gap caused by order-disorder effects and oxygen vacancies.[9,24,116,117] For the insulator system the temperature variation induced changes in the PL spectrum. There is a transition between 75–150 K characterized by band shifting and stabilization of the intensity. There is a shift from 2.38 eV at 75 K to 2.48 eV at 150 K, -ΔE = 100 meV, and a shift back to 2.39 eV at a higher temperature. The PL emissions in the present samples are related to the participation of several energy states, which are derived from the bulk, surface, and interface defects of both materials. The PL emission spectra were deconvoluted, Figure S3, and shows that at 150 K for the insulator system there is a shift of emission to higher energies with contributions of blue regions. For the metallic system changes in this region were not observed. This shift in the insulator system can be energetically explained using oxygen vacancies of types $V_O^{\cdot}$ and $V_O^{\cdot\cdot}$, which are mono- and doubly-ionized types, respectively. As mono-ionized vacancies present at ~ 80 meV below the conduction band, we considered that the insulator system showing ΔE = 100 meV between 10–150 K may represent this type of vacancy. Therefore, it is plausible to assume that the presence of these types of defects is significant to the charge transfer process at the oxide interface (2D gas), the scattering effects of the crystal lattice, and the strong electronic correlation in a perovskite structure.[53]

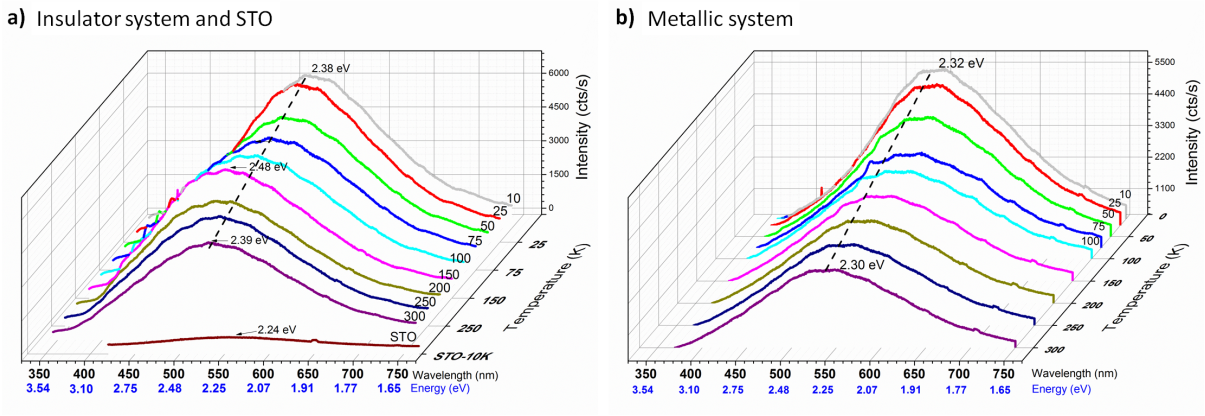

Figure 4. Degree of order and disorder related to the PL spectra obtained in the temperature range of 10 to 300 K. In (a), for the pure STO substrate and for the insulator system, at 150 K, there is an emission displacement related to the disordered state of the insulator system. In (b), the spectra related to the metallic system.

3.3 Joint theoretical and experimental analysis of the metallic interface formation process

The interface made by the co-exposed surfaces of $LaAlO_3/SrTiO_3$ was studied using an explicit atomistic model of the interface via density functional theory. The nature of the interface was evaluated by looking at the structure and considering the interfacial effects. The computational method, model systems, and technical details are given in the Supplementary Material.

As previously mentioned, the theoretical results reveal that the type of termination and interface plays an important role in the interaction between the LAO and STO surfaces. When the interaction occurs at an interface composed of $(LaO)^{+}-(SrO)^{0}$ layers (Figure S4a) or between the $(AlO_2)^{-}-(TiO_2)^{0}$ layers (Figure S4c), an increase in the interatomic distance is observed. However, when there is an interaction between $((LaO)^{+}-(TiO_2)^{0}$ or $(AlO_2)^{-}-(SrO)^{0})$ layers, a decrease in the interatomic distance occurs, resulting in a bond between the LAO and STO surface, as illustrated on Figures S4b and S4d. To verify the model in which it is possible

for free electrons to be present and the trapping of electrons to occur, the values of the Mulliken charge of each interface were calculated (Figures S5) for the models where we observed an increase in the interatomic distance. The LAO/STO heterostructure formed by the $(LaO)^{+}-(SrO)^{0}$ interface exhibits a negative charge (Figure S5a). This observation implies that there is a repulsive force between them, and the electrons can be repelled; consequently, the gas will be not formed. On the other hand, the LAO/STO heterostructure formed by the interaction on the $(AlO_2)^{-}-(TiO_2)^{0}$ interface (Figure S5b) provides a perfect environment for trapping electrons between both materials, as the positive charge of the clusters attracts the electrons.

In the 2D interface composed of $(AlO_2)^{-}-(TiO_2)^{0}$, the three-dimensional chemical environment will be formed by clusters, i.e., under-coordinated $[TiO_5]$ and $[AlO_5]$ clusters, which are displayed in Figure S4b. From these results, three more models were constructed to analyze the effect of excess O anions on the upper part of the heterostructure, simulating the experimental condition for the oxygenated system of the LAO/STO heterostructure. Figure 6a shows the model represented in Figure S4c with an excess of O atoms on the top of the LAO surface. The other two models are asymmetric (symmetric (asymmetric) model is when the bottom and top of the slab are with the same (different) termination of atoms) systems without excess oxygen (Figure 6b) and with excess oxygen (Figure 6c) on the top of LAO surface, which are related experimentally to the insulator (non-oxygenated) and metallic (oxygenated) system, respectively. The excess of O anions on top of the surfaces (Figures 6a and 6c) are capable of eliminating the oxygen vacancies that are present in the $[AlO_5]$ and $[LaO_8]$ cluster; then, a complete local coordination, $[AlO_6]$ and $[LaO_{12}]$ cluster, are formed. The Mulliken charge of the clusters was also calculated and is shown in Figure 6. From Figure 6a, it is possible to affirm that the excess of O atoms in the $[TiO_5]-[AlO_5]$ model does not significantly affect the Mulliken charge of this clusters, despite an increase occurring in the interatomic distance between the STO and LAO (100) surfaces. Unlike in the non-stoichiometry symmetric model

shown in Figure 6a, in the case of the non-oxygenated stoichiometric model, Figure 6b, with asymmetrical terminations, there is an increase in the Mulliken charge. This increase is a consequence of the structural and electronic disorder imposed by the stoichiometries that are capable of improving the capability of the environment to trap electrons on the interface of STO and LAO. For the oxygenated stoichiometry system, an increase in the values for the Mulliken charge of the clusters was also observed. These theoretical results reveal that, for 2DEG to be generated, the structure of STO and LAO on the (100) LAO/STO heterostructure needs to be formed by a stoichiometric system, as verified by the experimental relationship between Sr/Ti and the octahedral environment, and, as a consequence, by the asymmetrical terminations of the surface; furthermore, undercoordinated $[AlO_5]$ and $[TiO_5]$ clusters must be present on the interface. These asymmetrical terminations of the surface result in an increase in the disorder of the heterostructure, improving the formation of the 2DEG. This hinders recombination and is most likely the reason for the high electronic conductivity of the heterostructure.

From a thermodynamic point of view, the formation of defects can be explained by using energy criteria (cost to generate the defect) and entropy (how much is gained to generate the defect), as studied by Reinle-Schmitt et al.[118], who suggested that the 2DEG behavior originates from a stoichiometric layer between Sr/Ti and the insulating behavior of the LAO/STO interface, which is related to the presence of a layer rich in Sr. However, from our XPS results we observed that the ratios of Ti/Sr for both systems, oxygenated and non-oxygenated, are the same, but atomic interdiffusion is different in the two systems. This observation allows us to note that stoichiometry is not responsible for the 2DEG behavior; rather, it is the defects arising from the crystalline lattice former, Ti, which, according to *ab initio* calculations,[119] predict a considerable increase in the covalence of the Ti−O bond near the surface. Therefore, the presence of Ti cations seems to be responsible for the electronic structure of surface defects. The local coordination of the Ti cation in the cubic structure corresponds to the $[TiO_6]$ clusters. However, by means of spectroscopic measurements,[120,121] our group demonstrates the lowest

number of Ti−O coordination through $[TiO_5]$ clusters generated by the formation of oxygen vacancies (V_O^x). This was also confirmed by our theoretical calculations. We believe, through the PL results (ΔE = 100 meV) and studies already carried out by electron paramagnetic resonance spectroscopy,[112,116] that shallow defects can exist, i.e., at a few meV below the conduction band of an intrinsic type, such as an oxygen vacancy, as a result of energy variation. To achieve this state, the system interface is processed as described below, eq. 01. Kröger-Vink notation was used, where the superscript (x) indicates a neutral charge, symbol ($\bullet$) corresponds to a positive charge, and symbol ($'$) denotes a negative charge. The order and disorder clusters are represented by [ ]$_o$ and [ ]$_d$, respectively.

$$[TiO_6]_o^x + [TiO_5 \cdot V_O^x]_d \rightarrow [TiO_6]_d' + [TiO_5 \cdot V_O^\bullet]_d \quad \text{Eq. 01}$$

The interaction between the clusters leads to the formation of $[TiO_6]_d'$ clusters, the electron donor state, as shown in the eq. 02. An under-coordinated cluster is then formed. It will act as a donor state of the electrons for the system:

$$[TiO_6]_o^x + [TiO_4 \cdot 2V_O^x]_d \rightarrow [TiO_6]_d' + [TiO_4 \cdot V_O^x V_O^\bullet]_d \quad \text{Eq. 02}$$

The chemical environment for the interface region similar to the one described by the equation was also reported as being necessary for the formation of 2DEG, in which the Ti valency varies from +3 in the interface to +4 in bulk.[47] Thus, the degeneration of the orbitals, from octahedral to tetrahedral $[TiO_4 \cdot 2V_O^x]_d$ [47,122,123] in the interface region allied to $[TiO_4 \cdot V_O^x V_O^\bullet]_d$[31] results in the formation of electron donors. Therefore, the 2DEG behavior can be associated with the local chemical environment of the clusters of the upper part of the heterostructure, which according to binding energy analysis are mainly aluminum clusters. For

the non-oxygenated films, the system is obtained with lack of oxygen, as observed by XPS analysis; therefore, the aluminum clusters will tend to be accommodated in a tetrahedral environment. For this, the monoionized vacancies will appear in this system, thus allowing the capture or releasing electrons (eq. 03).

$$[AlO_6]'_d + [AlO_5 \cdot V_O^{\bullet}]_d \rightarrow [AlO_6]_o^x + [AlO_5 \cdot V_O^x]_d \qquad \text{Eq. 03}$$

In this case, although the defects remain in the structure, they are canceled out, and the 2DEG behavior is not observed. On the other hand, in cases where the 2DEG behavior is observed, the system passes through the oxygenation stage (eq. 04), which increases the diffusion of the Al cation by the structure, resulting in its diffusion to the upper part of the film. Therefore, it appears in high quantities, according to the XPS analysis, which results in the complexation of the clusters of aluminum into an octahedron with the oxygen of the system:

$$[AlO_5.V_o^x]_d + \frac{1}{2}O_2 \rightarrow [AlO_6]'_o \qquad \text{Eq. 04}$$

This process stabilizes the octahedral clusters, as was observed in the XPS analysis, preventing the capture of the electron from the interface and at the same time imprisoning it and thus resulting in the 2DEG behavior (eq. 05).

$$[TiO_4 \cdot 2V_O^x]_d + 2[AlO_6]_o^x \rightarrow [TiO_4 \cdot 2V_O^{\bullet}]_d + [AlO_6]'_d \qquad \text{Eq. 05}$$

From here, a cascade of processes can be performed at the interface (eq. 06), such as,

$$[TiO_4 \cdot 2V_O^x]_d \rightarrow [TiO_4 \cdot 2V_O^{\bullet\bullet}]_d + 4[AlO_6]'_d \qquad \text{Eq. 06}$$

Our first-principles calculations demonstrate the accumulation of electrons at the bottom *n*-type and the top *p*-type $(AlO_2)^-$–$(TiO_2)^0$ interface. Therefore, to realize 2DEG practically, we focus on two issues: (1) building an atomically-sharp p-type interface that consists of AlO_2/TiO_2 layers and (2) minimizing oxygen vacancies near the p-type interface, creating an adequate environment to trap electrons between both materials. Finally, we can also recover the orbital ordering of the mobile and localized electrons at oxygen-deficient LAO/STO interfaces, as it was employed, very recently, by Chikina et al.[49], to explain the formation and behavior of the 2DEG. In this interface, the octahedral crystal field with an oxygen vacancy, i.e., undercoordinated $[TiO_5]$ and $[AlO_5]$ clusters change the energy and occupancy of the t_{2g} and e_g states, and there is an exchange coupling process between the partially filled Tid_{xy} and half-filled Tie_g induced by the presence of oxygen vacancies at the interface.[14,124–128]

4. CONCLUSIONS

In summary, we have investigated the 2DEG properties at the LAO/STO interface synthetized using pulsed laser deposition under both non-oxygenated and oxygenated conditions. This work we have highlighted the structural chemistry of the A- and B-sites of perovskite materials, STO and LAO, with computational work indicating the possibility of tuning the interface and surfaces so that they are suitable for 2DEG formation. Their structure and electronic properties have been studied by different experimental techniques and complemented by a first principles DFT calculation, using explicit atomistic models of the interface. The relation among the structure, electronic, and magnetic properties of the LAO/STO interface is rationalized by considering the relative contribution of three structural aspects: oxygen vacancies; structural deformations (including cation disorder); and electronic and orbital interface reconstruction. Our results reveal the importance of oxygen defects at the interface and surface of the LAO/STO. These defects are directly related to the partial pressure

of oxygen during the preparation of the sample. Both experimental and theoretical results were employed to support our hypothesis, in which we propose the presence of undercoordinated $[TiO_5]$ and $[AlO_5]$ clusters of the co-exposed surfaces at the interface as key ingredient for 2DEG formation. Our study introduces the possibility of defect engineering through the manipulation of oxygen vacancies and facet control at the interface and surface of materials, which can be ultimately be helpful in understanding the formation mechanisms of 2DEG at metal oxide interfaces. We expect this new understanding will open up potential applications in future devices.

5. EXPERIMENTAL SECTION

Growth process of the LAO/STO heterojunction: For the deposition of the heterojunction, crystalline substrates of $SrTiO_3$ along the [100] direction were used. Surface treatments were performed on the substrates, based on the work of Koster et al.[129], for TiO_2 termination layers, and atomically flat $SrTiO_3$ surface was obtained, as confirmed by atomic force microscopy (Figure S1a). $LaAlO_3$ films were grown by the PLD method in an ultra-high *vacuum* chamber using a KrF excimer laser with a wavelength of 248 nm. The frequency used was 2 Hz, and the laser beam was incident at 45° to the normal target surface at a fluence of 1.8 J/cm^2. The deposition temperature was 730°C, and it was measured immediately on the back of the substrate fixed on the heater by a thermocouple. The base pressure was 10^{-9} mbar and the deposition pressure with continuous oxygen flow was 2×10^{-4} mbar. The distance between the target and the substrate was 4 cm. After LAO growth, the sample set was then calcined for 60 min at an oxygen partial pressure of 200 mbar at 550 °C, and then cooled at the same O_2 pressure to room temperature; this sample set was named “metallic”. An additional set of samples was not oxygenated and cooled to room temperature at the same deposition oxygen pressure; these samples were named “insulator”.

Characterization techniques: The surface were characterized by atomic force microscopy (AFM) (Digital Instruments, Model NanoScopeIIIa) using the tapping mode. Raman spectroscopy characterization was accomplished using aLabRAM iHR550 Horiba JobinYvon spectrometer with a 514-nm laser as the excitation source (spectral resolution of 1 cm^{-1}). X-ray diffraction (XRD) were performed with a diffractometer (Rigaku, Model Rint 2000). For surface characterization, X-ray photoelectron spectroscopy (XPS) measurements were obtained using a ScientaOmicron ESCA+spectrometer system equipped with a hemispherical analyzer (EA125) and a monochromatic source of Al Kα (hν = 1486.7 eV). The source was rated at 280W, while the spectrometer worked at a constant pass energy mode at 50eV. All data analyses were made using CASA XPS Software (Casa Software Ltd., UK). The spectra were analyzed by first performing a Shirley background subtraction and correcting the charge effects using the C1s peak of adventitious carbon at 285.0 eV as a reference. Peak fitting was performed using an asymmetric Gaussian–Lorentzian product function (for the peak shape) and maintaining the ratio between spin-orbit splitting components. PL measurements were performed using a commercial confocal microscope (Attocube/CFMI) compatible with low temperatures and high magnetic fields. The samples were excited by a 355-nm laser coupled into a single-mode optical fiber, with the beam focused onto the sample by an aspheric lens. The luminescence was collimated by the same lens and projected into a 50-μm multimode optical fiber dispersed by a 75-cm spectrometer (Andor-Shamrock) and detected by a charged couple device (AndoriDus).

Electrical and magnetic measurements: For electrical and magnetic measurements, the devices were fabricated to enable analysis of the transport properties at the substrate/film interface. A conventional lithography process was used for defining the active regions (10 μm-wide Ti/Au alloy parallel bars) on the surface of the film. In the second step, a focused ion beam (FIB) microscope was used to drill the surface of the films so that it would make direct contact with the interface. The devices were drilled by an electron beam to reach the LAO/STO interface,

and Pt was injected into the drilled holes in order contact with the 2DEG region according to a previous report[130]. Transport measurements were performed at different temperatures (8–300 K) using a closed-cycle He cryostat (Janis Research®, CCS150 model). The samples were maintained at a pressure lower than 5×10^{-6} mbar. The resistance was obtained using standard low frequency AC lock-in (13Hz) and DC techniques, but the results remained unchanged. We used different current levels in the experiments to avoid non-linear transport due to high-field effects and undesired Joule heating. Initial electrical characterization (current-voltage curves) showed a linear shape as expected. We also conducted four- and two-probe measurements in different samples, but the resistivity/resistance also remained unchanged in the entire temperature range. Magnetoresistance measurements were performed using a four-wire configuration connected to a source meter (Keithley, 2400C model) and placed inside an ultra-low vibration cryostat (Attocube, modelAttodry 1000) operating at 4 K. Amagnetic field up to 9 T was applied using Faraday geometry (perpendicular to the sample surface).

SUPPLEMENTARY MATERIAL

See the supplementary material for the AFM and XRD of samples preparing, and PL deconvolutions of Figure 5. The computational method, model systems, and technical details are also given in the Supplementary Material.

ACKNOWLEDGEMENTS

The authors acknowledge the CEPID/CDMF and the São Paulo Research Foundation (FAPESP) (Prof. Nos. 2013/07296-2, 2014/01371-5, 2017/23663-6, 2019/09296-6 and 2017/19143-7), National Council for Scientific and Technological Development (CNPq) (No 150949/2018-9), and the Coordenação de Aperfeiçoamento de Pessoal de Nível Superior (CAPES)for the financial support granted in the course of this research. We are also grateful to the LMA-IQ for providing the FEG-FIB-SEM facilities. The Brazilian authors acknowledge the financial support of the following Brazilian research financing institutions: CNPq

(150949/2018-9), FAPESP (2013/07296-2, 2017/19143-7 and 2019/09296-6), and CAPES. J.A. acknowledges the financial support from the Generalitat Valenciana for Prometeo II/2014/022, ACOMP/2015/1202, the Spanish Ministerio de Economia y Competitividad (MINECO), project CTQ2015-65207-P, Ministerio de Ciencia, Innovación y Universidades (Spain) project PGC2018-094417-B-I00 and Universitat Jaume I, project no. UJI-B2016-25.

REFERENCES

1 S. Thiel, G. Hammerl, A. Schmehl, C. W. Schneider and J. Mannhart, *Science (80-.).*, 2006, **313**, 1942–1945.

2 A. Ohtomo, D. A. Muller, J. L. Grazul and H. Y. Hwang, *Nature*, 2002, **419**, 378–80.

3 M. Huijben, G. Koster, M. K. Kruize, S. Wenderich, J. Verbeeck, S. Bals, E. Slooten, B. Shi, H. J. a. Molegraaf, J. E. Kleibeuker, S. van Aert, J. B. Goedkoop, A. Brinkman, D. H. a. Blank, M. S. Golden, G. van Tendeloo, H. Hilgenkamp and G. Rijnders, *Adv. Funct. Mater.*, 2013, **23**, 5240–5248.

4 H. Hilgenkamp, *MRS Bull.*, 2013, **38**, 1026–1031.

5 M. Ben Shalom, A. Ron, A. Palevski and Y. Dagan, *Phys. Rev. Lett.*, 2010, **105**, 1–4.

6 P. Moetakef, C. A. Jackson, J. Hwang, L. Balents, S. J. Allen and S. Stemmer, *Phys. Rev. B*, 2012, **86**, 201102.

7 R. Ghosh, D. Basak and S. Fujihara, *J. Appl. Phys.*, 2004, **96**, 2689.

8 A. Aezami, M. Abolhassani and M. Elahi, *J. Alloys Compd.*, 2014, **587**, 778–782.

9 V. M. Longo, L. S. Cavalcante, M. G. S. Costa, M. L. Moreira, A. T. de Figueiredo, J. Andrés, J. A. Varela and E. Longo, *Theor. Chem. Acc.*, 2009, **124**, 385–394.

10 R. A. C. Amoresi, V. Teodoro, G. F. Teixeira, M. S. Li, A. Z. Simões, L. A. Perazolli, E. Longo and M. A. Zaghete, *J. Eur. Ceram. Soc.*, 2018, **38**, 1621–1631.

11 H. Guo, W. A. Saidi, J. Yang and J. Zhao, *Nanoscale*, 2016, **8**, 6057–6063.

12 S. Thiel, G. Hammerl, A. Schmehl, C. W. Schneider and J. Mannhart, *Science*, 2006, **313**, 1942–5.

13 A. Ohtomo and H. Y. Hwang, *Nature*, 2004, **427**, 423–427.

14 A. Brinkman, M. Huijben, M. van Zalk, J. Huijben, U. Zeitler, J. C. Maan, W. G. van der Wiel, G. Rijnders, D. H. a Blank and H. Hilgenkamp, *Nat. Mater.*, 2007, **6**, 493–6.

15 N. Reyren, S. Thiel, a D. Caviglia, L. F. Kourkoutis, G. Hammerl, C. Richter, C. W. Schneider, T. Kopp, A.-S. Rüetschi, D. Jaccard, M. Gabay, D. a Muller, J.-M. Triscone and J. Mannhart, *Science*, 2007, **317**, 1196–9.

16 E. Lesne, Y. Fu, S. Oyarzun, D. C. Vaz, H. Naganuma, G. Sicoli, M. Jamet, E. Jacquet, A. Fert, M. Bibes and L. Vila, *Nat. Mater.*, 2016, **15**, 1261.

17 H. Lee, N. Campbell, J. Lee, T. J. Asel, T. R. Paudel, H. Zhou, J. W. Lee, B. Noesges, J. Seo, B. Park, L. J. Brillson, S. H. Oh, E. Y. Tsymbal, M. S. Rzchowski and C. B. Eom, *Nat. Mater.*, 2018, **17**, 231–236.

18 S. Stemmer and S. J. Allen, *Annu. Rev. Mater. Res.*, 2014, **44**, 151–171.

19 M. Huijben, G. Koster, M. K. Kruize, S. Wenderich, J. Verbeeck, S. Bals, E. Slooten, B. Shi, H. J. A. Molegraaf, J. E. Kleibeuker, S. Van, J. B. Goedkoop, A. Brinkman, D. H. A. Blank and M. S. Golden, *Adv. Funct. Mater.*, 2013, **23**, 5240–5248.

20 G. Li, W. Wang, W. Yang and H. Wang, *Surf. Sci. Rep.*, 2015, **70**, 380–423.

21 H. M. Christen and G. Eres, *J. Phys. Condens. Matter*, 2008, **20**, 264005.

22 L. Cichetto Jr., S. Sergeenkov, J. C. C. A. Diaz, E. Longo and F. M. Araujo-Moreira, *AIP Adv.*, , DOI:10.1063/1.4971842.

23 D. H. A. Blank, G. J. H. M. Rijnders, G. Koster and H. Rogalla, *J. Electroceramics*, 2000, **4**, 311–318.

24 Z. Q. Liu, C. J. Li, W. M. Lu, X. H. Huang, Z. Huang, S. W. Zeng, X. P. Qiu, L. S. Huang, A. Annadi, J. S. Chen, J. M. D. Coey and T. Venkatesan, *Phys. Rev. X*, 2013, **3**, 21010.

25 P. R. Willmott, S. A. Pauli, R. Herger, C. M. Schlep??tz, D. Martoccia, B. D. Patterson, B. Delley, R. Clarke, D. Kumah, C. Cionca and Y. Yacoby, *Phys. Rev. Lett.*, 2007, **99**, 155502.

26 J. E. Hamann-borrero, S. Macke, W. S. Choi, R. Sutarto, F. He, A. Radi, I. Elfimov, R. J. Green, M. W. Haverkort, V. B. Zabolotnyy, H. N. Lee, G. A. Sawatzky and V. Hinkov, *npj Quantum Mater.*, 2016, **1**, 16013.

27 H. Y. Hwang, Y. Iwasa, M. Kawasaki, B. Keimer, N. Nagaosa and Y. Tokura, *Nat. Publ. Gr.*, 2012, **11**, 103–113.

28 C. Richter, H. Boschker, W. Dietsche, R. Jany, F. Loder, L. F. Kourkoutis, D. A. Muller, J. R. Kirtley, C. W. Schneider and J. Mannhart, *Nature*, 2013, **502**, 528–531.

29 A. J. Millis, *Nat. Phys.*, 2011, **7**, 749–750.

30 S. Banerjee, O. Erten and M. Randeria, *Nat. Phys.*, 2013, **9**, 626–630.

31 M. Salluzzo, S. Gariglio, D. Stornaiuolo, V. Sessi, S. Rusponi, C. Piamonteze, G. M. De Luca and M. Minola, *Phys. Rev. Lett.*, 2013, **111**, 087204_1-5.

32 D. A. Dikin, M. Mehta, C. W. Bark, C. M. Folkman, C. B. Eom and V. Chandrasekhar, *Phys. Rev. Lett.*, 2011, **107**, 56802.

33 L. Li, C. Richter, J. Mannhart and R. C. Ashoori, *Nat. Phys.*, 2011, **7**, 762–766.

34 P. Perna, D. Maccariello, M. Radovic, I. Pallecchi, M. Codda, J. Gazquez, M. Varela, S. J. Pennycook and F. M. Granozio, *Appl. Phys. Lett.*, 2010, **97**, 152111.

35 A. Annadi, A. Putra, Z. Q. Liu, X. Wang, K. Gopinadhan, Z. Huang, S. Dhar, T. Venkatesan and Ariando, *Phys. Rev. B - Condens. Matter Mater. Phys.*, 2012, **86**, 1–5.

36 U. Treske, N. Heming, M. Knupfer, B. Büchner, E. Di Gennaro, A. Khare, U. Scotti, D. Uccio, F. M. Granozio, S. Krause and A. Koitzsch, *Nat. Publ. Gr.*, 2015, **5**, 14506.

37 C. Li, Z. Liu, W. Lu, X. R. Wang, A. Annadi, Z. Huang, S. Zeng and T. Venkatesan, *Sci. Rep.*, 2015, **5**, 13314.

38 P. Xu, W. Han, P. M. Rice, J. Jeong, M. G. Samant, K. Mohseni, H. L. Meyerheim, S.

Ostanin, I. V Maznichenko, I. Mertig, E. K. U. Gross, A. Ernst and S. S. P. Parkin, *Adv. Mater.*, 2017, **29**, 1604447.

39 Y. Pai, A. Tylan-tyler, P. Irvin and J. Levy, *Reports Prog. Phys.*, 2018, **81**, 36503.

40 H. Guo, W. A. Saidi and J. Zhao, *Phys. Chem. Chem. Phys.*, 2016, **18**, 28474–28484.

41 F. Zhang, Y. Fang, N. Y. Chan, W. C. Lo and D. F. Li, *Phys. Rev. B*, 2016, **93**, 214427.

42 L. Wang, W. Pan, W. X. Hu and D. Y. Sun, *Phys. Chem. Chem. Phys.*, 2019, **21**, 7075–7082.

43 N. Pavlenko, T. Kopp, E. Y. Tsymbal, J. Mannhart and G. A. Sawatzky, *Phys. Rev. B*, 2012, **86**, 64431.

44 V. Vonk, J. Huijben, D. Kukuruznyak, A. Stierle, H. Hilgenkamp, A. Brinkman and S. Harkema, *Phys. Rev. B*, 2012, **85**, 45401.

45 R. Pentcheva and W. E. Pickett, *J. Phys. Condens. Matter*, 2010, **22**, 43001.

46 G. Herranz, F. Sanchez, N. Dix, M. Scigaj and J. Fontcuberta, *Sci. Rep.*, 2012, **2**, 758.

47 A. Chikina, F. Lechermann, M. Husanu, M. Caputo, C. Cancellieri, X. Wang, T. Schmitt, M. Radovic and V. N. Strocov, *ACS Nano*, 2018, **12**, 7927–7935.

48 N. Nakagawa, H. Y. Hwang and D. A. Muller, *Nat. Mater.*, 2006, **5**, 204–209.

49 C. F. Chang, Z. Hu, S. Klein, X. H. Liu, R. Sutarto, A. Tanaka, J. C. Cezar, N. B. Brookes, H. Lin, H. H. Hsieh, C. T. Chen, A. D. Rata and L. H. Tjeng, *Phys. Rev. X*, 2016, **6**, 41011.

50 I. Tung, G. Luo, J. H. Lee, S. H. Chang, J. Moyer, H. Hong, M. J. Bedzyk, H. Zhou, D. Morgan, D. D. Fong and J. W. Freeland, *Phys. Rev. Mater.*, 2017, **1**, 53404.

51 Y. Kim, A. Morozovska, E. Eliseev, M. P. Oxley, R. Mishra, S. M. Selbach, T. Grande, S. T. Pantelides, S. V Kalinin and A. Y. Borisevich, *Nat. Mater.*, 2014, **13**, 1019–1025.

52 F. Y. Bruno, M. N. Grisolia, C. Visani, S. Valencia, M. Varela, R. Abrudan, J. Tornos, S. J. Pennycook, Z. Sefrioui, C. Leon, J. E. Villegas and J. Santamaria, *Nat. Commun.*, 2015, **6**, 6306.

53 Y. Chen and R. J. Green, *Adv. Mater. Interfaces*, 2019, **1900547**, 1–15.

54 F. Wang, J. Li, X. Zhang, J. Liu, M. Zhao, W. Su, C. Wang and L. Mei, *Comput. Mater. Sci.*, 2018, **147**, 87–94.

55 H. Banerjee, S. Banerjee, M. Randeria and T. Saha-Dasgupta, *Sci. Rep.*, 2016, **5**, 18647.

56 R. Pentcheva and W. Pickett, *Phys. Rev. Lett.*, 2009, **102**, 107602.

57 W. Son, E. Cho, J. Lee and S. Han, *J. Phys. Condens. Matter*, 2010, **22**, 315501.

58 A. Janotti, L. Bjaalie and L. Gordon, *Phys. Rev. B*, 2012, **86**, 241108.

59 L. Zhang, X. Zhou, H. Wang, J. Xu, J. Li, E. G. Wang and S. Wei, *Phys. Rev. B*, 2010, **82**, 125412.

60 L. Weston, X. Y. Cui, S. P. Ringer and C. Stampfl, *Phys. Rev. Lett.*, 2014, **113**, 186401.

61 H. Hu, L. Ao, A. Pham, D. Wang, Y. Wang, Z. Chen, C. Kong, T. T. Tan, X. Zu and S. Li, *Adv. Mater. Interfaces*, 2016, **3**, 1600547.

62 J. Cheng, S. Nazir and K. Yang, *ACS Appl. Mater. Interfaces*, 2016, **8**, 31959–31967.

63 Y. Du, C. Wang, J. Li, X. Zhang, F. Wang, Y. Zhu, N. Yin and L. Mei, *Comput. Mater. Sci.*, 2015, **99**, 57–61.

64 A. Sorokine, D. Bocharov, S. Piskunov and V. Kashcheyevs, *Phys. Rev. B*, 2012, **86**, 155410.

65 D. Marton and J. W. Rabalais, *J. Chem. Phys.*, 1998, **108**, 1645–1652.

66 J. Li, W. Wu, Y. Shen, P. Zhang, Y. Hong, H. Bai and G. Li, *Comput. Theor. Chem.*, 2019, **156**, 286–291.

67 M. Behtash, S. Nazir, Y. Wang and K. Yang, *Phys. Chem. Chem. Phys.*, 2016, **18**, 6831–6838.

68 J. Cho, H. Jeen and E. Cho, *Thin Solid Films*, 2018, **651**, 13–17.

69 S. J. Leake, S. A. Pauli, C. Cancellieri, D. Fontaine, S. Gariglio, N. Reyren, A. D.

Caviglia and A. Fe, *Phys. Rev. Lett.*, 2011, **107**, 56102.

70 Y. B. Xue, Y. Y. Shan and H. Xu, *Comput. Mater. Sci.*, 2018, **149**, 354–359.

71 I. V Maznichenko, S. Ostanin, V. K. Dugaev, I. Mertig and A. Ernst, *Phys. Rev. Mater.*, 2018, **2**, 74003.

72 L. Guan, F. Tan, G. Shen, Y. Liang, X. Xu and J. Guo, *Appl. Surf. Sci.*, 2019, **475**, 185–190.

73 A. Kalabukhov, R. Gunnarsson, J. Börjesson, E. Olsson, T. Claeson and D. Winkler, *Phys. Rev. B - Condens. Matter Mater. Phys.*, 2007, **75**, 121404(R).

74 M. Bibes, C. Carre, G. Herranz and M. Basletic, *Phys. Rev. Lett.*, 2007, **98**, 216803.

75 W. Siemons, G. Koster, H. Yamamoto, W. A. Harrison, G. Lucovsky, T. H. Geballe, D. H. A. Blank and M. R. Beasley, *Phys. Rev. Lett.*, 2007, **98**, 196802.

76 C. Cen, S. Thiel, G. Hammerl, C. W. Schneider, K. E. Andersen, C. S. Hellberg, J. Mannhart and J. Levy, *Nat. Mater.*, 2008, **7**, 298–302.

77 L. Qiao, T. C. Droubay, T. C. Kaspar, P. V Sushko and S. A. Chambers, *Surf. Sci.*, 2011, **605**, 1381–1387.

78 S. A. Chambers, M. H. Engelhard, V. Shutthanandan, Z. Zhu, T. C. Droubay, L. Qiao, P. V. Sushko, T. Feng, H. D. Lee, T. Gustafsson, E. Garfunkel, A. B. Shah, J. M. Zuo and Q. M. Ramasse, *Surf. Sci. Rep.*, 2010, **65**, 317–352.

79 H. Zaid, M. H. Berger, D. Jalabert, M. Walls, R. Akrobetu, I. Fongkaew, W. R. L. Lambrecht, N. J. Goble, X. P. A. Gao, P. Berger and A. Sehirlioglu, *Sci. Rep.*, 2016, **6**, 28118.

80 Y.-L. Du, C.-J. Ji, X.-M. Zhang, C.-L. Li and X.-N. Fang, *Phys. Chem. Chem. Phys.*, 2019, **21**, 18170–18178.

81 F. Gunkel, S. Wicklein, S. Hoffmann-Eifert, P. Meuffels, P. Brinks, M. Huijben, G. Rijnders, R. Waser and R. Dittmann, *Nanoscale*, 2015, **7**, 1013–1022.

82 E. Frantzeskakis, T. Chris, F. Fortuna and A. F. Santander-syro, *J. Electron Spectros.*

Relat. Phenomena, 2017, **219**, 16–28.

83 L. Qiao, T. C. Droubay, T. Varga, M. E. Bowden, V. Shutthanandan, Z. Zhu, T. C. Kaspar and S. A. Chambers, *Phys. Rev. B*, 2011, **83**, 85408.

84 Y. Segal, J. H. Ngai, J. W. Reiner, F. J. Walker and C. H. Ahn, *Phys. Rev. B*, 2009, **80**, 241107.

85 R. Pentcheva and W. E. Pickett, *Phys. Rev. B*, 2006, **74**, 35112.

86 J. Tang, J. Zhu, W. Qin, J. Xiong, Y. Zhang and Y. Li, *Phys. Lett. A*, 2007, **365**, 149–155.

87 J. Goniakowski, F. Finocchi and C. Noguera, *Reports Prog. Phys.*, 2008, **71**, 16501.

88 P. Xu, Y. Ayino, C. Cheng, V. S. Pribiag, R. B. Comes, P. V Sushko, S. A. Chambers and B. Jalan, *Phys. Rev. Lett.*, 2016, **117**, 106803.

89 C. W. Bark, D. A. Felker, Y. Wang, Y. Zhang, H. W. Jang, C. M. Folkman, J. W. Park, S. H. Baek, H. Zhou, D. D. Fong, Q. Pan, E. Y. Tsymbal, M. S. Rzchowski and C. B. Eom, *Appl. Phys. Sci.*, 2011, **108**, 4720–4724.

90 N. C. Bristowe, P. Ghosez and P. B. Littlewood, *J. Phys. Condens. Matter*, 2014, **26**, 143201.

91 C. W. Schneider, S. Thiel, G. Hammerl, C. Richter, J. Mannhart, C. W. Schneider, S. Thiel, G. Hammerl, C. Richter and J. Mannhart, *Appl. Phys. Lett.*, 2006, **89**, 122101.

92 A. J. Chiquito, A. J. C. Lanfredi and E. R. Leite, *Phys. E Low-Dimensional Syst. Nanostructures*, 2008, **40**, 449–451.

93 A. Kalabukhov, Y. A. Boikov, I. T. Serenkov, V. I. Sakharov, J. Börjesson, N. Ljustina, E. Olsson, D. Winkler and T. Claeson, *Epl*, 2011, **93**, 37001.

94 X. Renshaw Wang, L. Sun, Z. Huang, W. M. Lü, M. Motapothula, A. Annadi, Z. Q. Liu, S. W. Zeng, T. Venkatesan and Ariando, *Sci. Rep.*, 2016, **5**, 18282.

95 I. M. Lifshitz and G. Peshanski, *Sov. Phys. JETP*, 1959, **35**, 875–883.

96 A. A. Abrikosov, *Sov. Phys. JETP*, 1969, **29**, 746–753.

97 G. Drera, G. Salvinelli, A. Brinkman, M. Huijben, G. Koster, H. Hilgenkamp, G. Rijnders, D. Visentin and L. Sangaletti, *Phys. Rev. B*, 2013, **87**, 75435.

98 C. Palacio and a. Arranz, *J. Phys. Chem. B*, 2001, **105**, 10805–10811.

99 a Mekki, D. Holland, K. Ziq and C. F. Mcconville, *J. Non. Cryst. Solids*, 1997, **220**, 267–279.

100 Z. Zhou, Y. Zhang, Z. Wang, W. Wei, W. Tang, J. Shi and R. Xiong, *Appl. Surf. Sci.*, 2008, **254**, 6972–6975.

101 J. J. Benitez, A. Diaz, Y. Laurent and J. A. Odriozola, 1998, **8**, 687–691.

102 T. T. P. Cheung, K. W. Willcox, M. P. McDaniel and M. M. Johnson, *J. Catal.*, 1986, **20**, 10–20.

103 M. Takizawa, S. Tsuda, T. Susaki, H. Y. Hwang and A. Fujimori, *Phys. Rev. B - Condens. Matter Mater. Phys.*, 2011, **84**, 3–7.

104 P. W. Lee, V. N. Singh, G. Y. Guo, H.-J. Liu, J.-C. Lin, Y.-H. Chu, C. H. Chen and M.-W. Chu, *Nat. Commun.*, 2016, **7**, 12773.

105 E. Slooten, Z. Zhong, H. J. A. Molegraaf, P. D. Eerkes, S. de Jong, F. Massee, E. van Heumen, M. K. Kruize, S. Wenderich, J. E. Kleibeuker, M. Gorgoi, H. Hilgenkamp, A. Brinkman, M. Huijben, G. Rijnders, D. H. A. Blank, G. Koster, P. J. Kelly and M. S. Golden, *Phys. Rev. B*, 2013, **87**, 85128.

106 A. Koitzsch, J. Ocker, M. Knupfer, M. C. Dekker, K. Dorr, B. Buchner and P. Hoffmann, *Phys. Rev. B - Condens. Matter Mater. Phys.*, 2011, **84**, 245121.

107 I. T. Chashechnikova, V. M. Vorotyntsev, V. V. Borovik, G. I. Golodets, I. V. Plyuto and A. P. Shpak, *Theor. Exp. Chem.*, 1993, **28**, 176–178.

108 B. Bharti, S. Kumar, H.-N. Lee and R. Kumar, *Sci. Rep.*, 2016, **6**, 32355.

109 P. T. Hsieh, Y. C. Chen, K. S. Kao and C. M. Wang, *Appl. Phys. A Mater. Sci. Process.*, 2008, **90**, 317–321.

110 S. Sonsupap, P. Kidkhunthod, N. Chanlek, S. Pinitsoontorn and S. Maensiri, *Appl.*

Surf. Sci., 2016, **380**, 16–22.

111 J. Miao, J. Sunarso, C. Su, W. Zhou, S. Wang and Z. Shao, *Sci. Rep.*, 2017, **7**, 44215.

112 G. Zhang, W. Jiang, S. Hua, H. Zhao, L. Zhang and Z. Sun, *Nanoscale*, 2016, **8**, 16963–16968.

113 J. A. Enterkin, A. K. Subramanian, B. C. Russell, M. R. Castell, K. R. Poeppelmeier and L. D. Marks, *Nat. Mater.*, 2010, **9**, 245–248.

114 M. L. Moreira, M. F. C. Gurgel, G. P. Mambrini, E. R. Leite, P. S. Pizani, J. A. Yarda and E. Longo, *J. Phys. Chem. A*, 2008, **112**, 8938–8942.

115 L. Gracia, J. Andrés, V. M. Longo, J. A. Varela and E. Longo, *Chem. Phys. Lett.*, 2010, **493**, 141–146.

116 V. M. Longo, A. T. De Figueiredo, S. De Lázaro, M. F. Gurgel, M. G. S. Costa, C. O. Paiva-Santos, J. A. Varela, E. Longo, V. R. Mastelaro, F. S. De Vicente, A. C. Hernandes and R. W. A. Franco, *J. Appl. Phys.*, 2008, **104**, 23515.

117 J. Q. Chen, X. Wang, Y. H. Lu, A. Roy Barman, G. J. You, G. C. Xing, T. C. Sum, S. Dhar, Y. P. Feng, Q. H. Xu and T. Venkatesan, *Appl. Phys. Lett.*, 2011, **98**, 41904.

118 M. L. Reinle-Schmitt, C. Cancellieri, A. Cavallaro, G. F. Harrington, S. J. Leake, E. Pomjakushina, J. A. Kilner and P. R. Willmott, *Nanoscale*, 2014, **6**, 2598.

119 E. Heifets, R. I. Eglitis, E. A. Kotomin, J. Maier and G. Borstel, *Phys. Rev. B*, 2001, **64**, 235417.

120 L. F. da Silva, W. Avansi, J. Andrés, C. Ribeiro, M. L. Moreira, E. Longo and V. R. Mastelaro, *Phys. Chem. Chem. Phys.*, 2013, **15**, 12386.

121 F. . Pontes, E. Longo, E. . Leite, E. J. . Lee, J. . Varela, P. . Pizani, C. E. . Campos, F. Lanciotti, V. Mastellaro and C. . Pinheiro, *Mater. Chem. Phys.*, 2002, **77**, 598–602.

122 K. P. Rajeev, G. V. Shivashankar and A. K. Raychaudhuri, *Solid State Commun.*, 1991, **79**, 591–595.

123 M. Yang, Ariando, J. U. N. Zhou, T. C. Asmara, P. Krueger, X. J. Yu, X. Wang, C.

Sanchez-Hanke, Y. P. Feng, T. Venkatesan and A. Rusydi, *ACS Appl. Mater. Interfaces*, 2018, **10**, 9774–9781.

124 Ariando, X. Wang, G. Baskaran, Z. Q. Liu, J. Huijben, J. B. Yi, A. Annadi, A. R. Barman, A. Rusydi, S. Dhar, Y. P. Feng, J. Ding, H. Hilgenkamp and T. Venkatesan, *Nat. Commun.*, 2011, **2**, 188.

125 Z. Salman, O. Ofer, M. Radovic, H. Hao, K. H. Chow, M. D. Hossain, C. D. P. Levy, W. A. Macfarlane, G. M. Morris, L. Patthey, M. R. Pearson, H. Saadaoui, T. Schmitt, D. Wang and R. F. Kiefl, *Phys. Rev. Lett.*, 2012, **109**, 257207.

126 B. Kalisky, J. A. Bert, B. B. Klopfer, C. Bell, H. K. Sato, M. Hosoda, Y. Hikita, H. Y. Hwang and K. A. Moler, *Nat. Commun.*, 2012, **3**, 922.

127 F. Lechermann, L. Boehnke, D. Grieger and C. Piefke, *Phys. Rev. B*, 2014, **90**, 85125.

128 M. Behrmann and F. Lechermann, *Phys. Rev. B*, 2015, **92**, 125148.

129 G. Koster, B. L. Kropman, G. J. H. M. Rijnders, D. H. A. Blank and H. Rogalla, *Appl. Phys. Lett.*, 1998, **73**, 2920–2922.

130 R. A. C. Amoresi, L. Cichetto, S. Kundu, M. D. Teodoro, G. E. Marques, E. Longo, J. Andrés, A. J. Chiquito, M. A. Zaghete, S. Kundu, M. D. Teodoro and R. A. C. Amoresi, *Appl. Phys. Lett.*, 2018, **113**, 131603.